Identifying Iron-Bearing Nanoparticle Precursor for Thermal Transformation into the Highly Active Hematite Photo-Fenton Catalyst

Anna Šutka [1], Andris Šutka [2,3,4,*] , Mārtiņš Vanags [2], Arnita Spule [2], Raivis Eglītis [2], Svetlana Vihodceva [2], Krišjānis Šmits [5], Aile Tamm [4] and Linda Mežule [6]

[1] Biomaterials Research Laboratory, Institute of Inorganic Chemistry, Faculty of Materials Science and Applied Chemistry, Riga Technical University, Paula Valdena 3/7, 1048 Riga, Latvia; anna.sutka@rtu.lv

[2] Research Laboratory of Functional Materials Technologies, Faculty of Materials Science and Applied Chemistry, Riga Technical University, Paula Valdena 3/7, 1048 Riga, Latvia; Martins.Vanags_4@rtu.lv (M.V.); arnita.spule@rtu.lv (A.S.); raivis.eglitis_1@rtu.lv (R.E.); Svetlana.Vihodceva@rtu.lv (S.V.)

[3] Institute of Atomic physics and spectroscopy, University of Latvia, Skunu 4, 1050 Riga, Latvia

[4] Institute of Physics, University of Tartu, W. Ostwaldi Street 1, 50411 Tartu, Estonia; aile.tamm@ut.ee

[5] Institute of Solid State Physics, University of Latvia, Kengaraga 8, LV-1063 Riga, Latvia; smits@cfi.lu.lv

[6] Water Research Laboratory, Faculty of Civil Engineering, Riga Technical University, Paula Valdena 1, 1048 Riga, Latvia; linda.mezule@rtu.lv

* Correspondence: andris.sutka@rtu.lv; Tel.: +371-26-138-155

Abstract: The hematite photo-Fenton catalysis has attracted increasing attention because it offers strong oxidation of organic pollutants under visible light at neutral pH. In the present work, aqueous synthesis of hematite photo-Fenton catalysts with high activity is demonstrated. We compare photo-Fenton activity for hematite obtained by hydrolyzation at 60 °C or by a thermally induced transformation from iron-bearing nanoparticles, such as amorphous iron oxyhydroxide or goethite. A link between their structure and visible light photo-Fenton reactivity is established. The highest activity was observed for hematite obtained from goethite nanowires due to oblong platelet-like structure, high surface area and the presence of nanopores.

1. Introduction

The number of published research works devoted to the heterogeneous photo-Fenton advanced oxidation process (AOP) has been drastically increasing in the last few years. This is because abundant non-toxic iron oxide-based catalysts can be used and the water treatment process can be driven by visible light. Moreover, contrary to homogeneous Fenton reaction which occurs under acidic conditions [1], the photo-Fenton reaction can be driven at neutral pH, thus avoiding the use of acids for triggering a reaction and bases for the neutralization afterward, as well as the formation of iron sludge by-product. In the heterogeneous photo-Fenton process, the photoexcited iron compound reacts with H_2O_2 and forms different reactive oxygen species (ROS), such as hydroxyl, hydroperoxyl and superoxide radicals following Equations (1)–(8) [2,3]. The superoxide radical is especially important to destroy persistent organic pollutants in water. The reduction potential of photoinduced electrons in hematite is not high enough to produce superoxide radical directly from oxygen, but in photo-Fenton

reaction with H_2O_2 superoxide, radicals could be produced by Equations (7) and (8). However, in the photo-Fenton process, the dominating ROS generated from H_2O_2 is $OH^\bullet$ [2].

$$Fe_2O_3 \xrightarrow{h\vartheta} Fe_2O_3\left(h^+ + e^-\right) \tag{1}$$

$$Fe^{3+} + e^- \rightarrow Fe^{2+} \tag{2}$$

$$Fe^{2+} + H_2O_2 \rightarrow Fe^{3+} + OH^\bullet + OH^- \tag{3}$$

$$H_2O_2 + e^- \rightarrow OH^\bullet + OH^- \tag{4}$$

$$H_2O + h^+ \rightarrow OH^\bullet + H^+ \tag{5}$$

$$h^+ + OH^- \rightarrow OH^\bullet \tag{6}$$

$$OH^\bullet + H_2O_2 \rightarrow H_2O + HO_2^\bullet \tag{7}$$

$$HO_2^\bullet \rightarrow O_2^{-\bullet} + H^+ \tag{8}$$

Different materials for heterogeneous photo-Fenton catalysts have been reported, such as α-,β-,γ-Fe_2O_3 [4–8], Fe_3O_4 [9], FeO [9], α-,β-FeOOH [10,11], $LaFeO_3$ [12], $BiFeO_3$ [13], $Fe_2(MeO_4)_3$ [3] and spinel ferrites MFe_2O_4 (where M is divalent metal cation) [14,15]. Additionally, the catalytic activity towards photo-Fenton reaction can be enhanced by synthesizing heterostructures with metals [2], metal oxides [16] and graphitic C_3N_4 [17]. The photoinduced charges are spatially separated over nanoheterostructures, thus decreasing the recombination rate [16]. Among all photo-Fenton catalysts, the hematite is especially attractive because a large variety of straightforward synthesis approaches can be used. Hematite is chemically stable and non-toxic. More importantly, hematite shows photo-Fenton catalytical activity in neutral conditions and under visible light [5,18]. Besides, the hematite has a highly positive valence band maximum potential resulting in a strong oxidation power of photogenerated holes, which could be suitable for direct organic pollution degradation [19]. Complex iron oxides, such as spinel ferrites, for example, shows photo-Fenton activity under acidic conditions [15]. Acidic conditions may trigger iron oxides or oxyhydroxides to dissolve and leach iron, thus decreasing stability and reducing activity [20].

The heterogeneous photo-Fenton catalytic activity of hematite is determined by surface exposed crystal facets [5], area and geometric shape [6]. The higher heterogeneous photo-Fenton catalytic activity is reported for {110} facets due to the higher density of unsaturated surface iron cations bonded to five oxygen [5]. Higher activity of hematite nanocrystals with the dominant {110} facets exposed to the surface could also be related to the higher density of Fe atoms on a plane [21].

Another approach to control the properties of desired target materials is to use different nanoparticle precursors [22]. Hematite can be obtained by thermal phase transformation from a large variety of iron-bearing nanoparticles, i.e., oxides and oxyhydroxides, because it is the thermal transformation final product for most of them [23]. However, the photo-Fenton activity for hematite nanoparticles obtained by a thermal transformation from various iron-bearing nanoparticle precursors has not yet been studied so far. At the same time, there are broad research possibilities because several nanoparticle shapes have been synthesized for iron oxides and oxyhydroxides, for example, nanoplates [24], nanowires [25], nanostructured urchin-like hollow spheres [26] and nanotubes [27]. This allows one to potentially obtain a large variety of different hematite nanostructures, with a potential to produce highly active photo-Fenton catalysts. In the present study, we are investigating photo-Fenton activity for hematite obtained directly by hydrolyzation at room temperature or by thermally induced structural transformation of iron oxyhydroxide amorphous nanoparticles or goethite nanowires. During the heating of all oxyhydroxides, dehydroxylation occurs alongside with thermal transformation to hematite. Due to the expulsion of water, nanopores are formed, thus increasing the specific surface area [23]. This resulted in the formation of a highly active hematite photo-Fenton nanocatalyst.

2. Results and Discussions

2.1. The Crystalline Structure and Morphology of Iron-Bearing Nanoparticle Precursors and Photo-Fenton Catalysts

The photo-Fenton hematite nanoparticle catalysts were obtained by a thermal transformation from various iron-bearing nanoparticle precursors or by direct hydrolyzation of iron (iii) nitrate at room temperature.

Amorphous FeO(OH) precursor was obtained by using HMTA as a precipitating agent as described before [28]. No peaks related to crystalline phases were observed in amorphous iron-containing precipitates, as shown by XRD studies (Figure 1). As it is demonstrated in SEM images in Figure 2a, the amorphous iron-containing precipitated particles have a non-uniform spherical shape, with sizes from 38 nm to 85 nm. The amorphous nanoparticles are packed in dense agglomerates. After annealing, the amorphous precipitates are transformed into the hematite phase (ICDD 04-006-0285) as indicated by XRD (Figure 1) and particles have grown to larger sizes from 89 nm to 264 nm as seen from SEM image (Figure 2b).
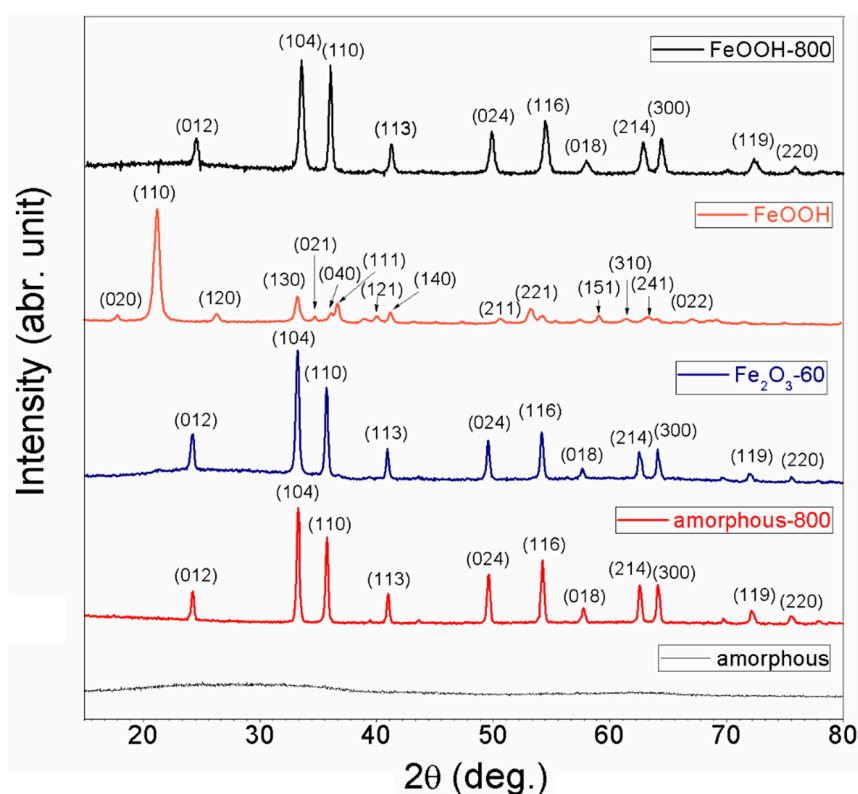

Figure 1. The XRD patterns of synthesized samples: amorphous—amorphous iron-containing precipitates; amorphous-800—hematite obtained from amorphous iron-containing precipitates after annealing at 800 °C; Fe_2O_3-60—synthesized by hydrolysis directly from solution at 60 °C; FeOOH—goethite α-FeOOH synthesized directly from solution at 60 °C; FeOOH-800—hematite obtained from goethite after annealing at 800 °C.

Single-phase goethite precursor was synthesized by precipitation using NaOH at pH > 12 as clearly indicated by powder XRD studies (Figure 1). Diffractograms exhibit strong peaks related to the goethite phase (ICDD 04-015-2899). No impurity phases were observed. As expected, precipitated goethite particles have a one-dimensional nanowire shape with length from 270 nm to 470 nm and diameter from 10 nm to 30 nm as seen from SEM image Figure 2c. TEM image for goethite precipitates (ESI Figure S1) shows that the majority of nanowires are grouped in bundles. The diameter of a single nanowire is around 20 ± 5 nm. Annealing transforms goethite to hematite (ICDD 04-006-0285),

as indicated by XRD (Figure 1), while simultaneously keeping the one-dimensional shape, as seen from SEM image (Figure 2d). After closer examination by TEM (Figure 2f), the hematite particles obtained from goethite contain pores. This is due to the expulsion of water during the transformation by Equation (9) [23]. The nanosized pores were not observed by TEM for bare α-FeOOH (ESI Figure S1). The nanosized pores increase the specific surface area, thus providing more active sites for the catalytic reaction. More interestingly, the α-FeOOH nanowires, during the transformation to hematite, are adapting a two-dimensional nanoplatelet shape as noticeable from SEM image (Figure 2d) and clearly visible in TEM images taken from different angles (Figure 2f).

$$2FeOOH \xrightarrow{t} Fe_2O_3 + H_2O \qquad (9)$$
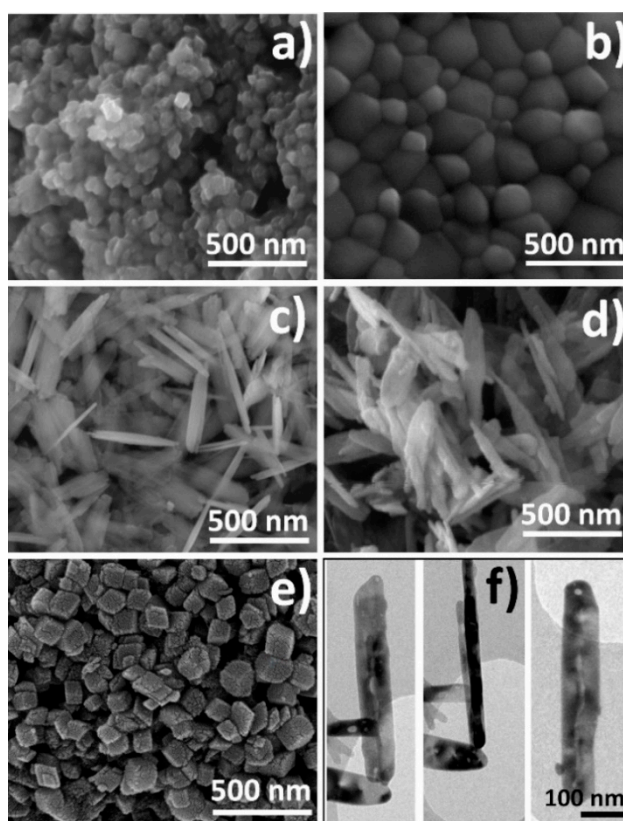
Figure 2. SEM images: (**a**) amorphous iron-containing precipitates, (**b**) hematite obtained from amorphous iron-containing precipitates after annealing at 800 °C, (**c**) goethite α-FeOOH synthesized directly from solution at 60 °C, (**d**) hematite obtained from goethite after annealing at 800 °C, (**e**) hematite synthesized by hydrolysis directly from solution at 60 °C. TEM images (**f**): hematite obtained from goethite after annealing at 800 °C—the images on left and the middle has been taken at different angles to prove the nanoplatelet morphology and image on the right clearly shows formation of nanopores into the structure.

Finally, the hematite α-Fe$_2$O$_3$ photo-Fenton catalysts were obtained directly from solution at 60 °C. The hematite formation in water under acidic conditions pH < 2.8 is well reported [29]. The iron polynuclear is first formed in the aqueous solution by adding NaOH but keeping conditions acidic. This polynuclear is further rearranged and transformed into hematite [30]. The XRD studies confirm monophasic α-Fe$_2$O$_3$ (ICDD 04-008-7623) formation directly from solution at 60 °C after 72 h. The SEM images (Figure 2e) show that the sizes of the obtained individual hematite particles are well below 10 nm and, upon drying, are self-assembled in secondary cube-like particles, with sizes from 100 to 266 nm.

The important parameter which influences the catalytic activity of the materials is the specific surface area (σBET), which was studied for all samples under study. The amorphous iron-containing nanoparticles exhibit the highest σBET—115.7 m^2/g. After annealing, the σBET for amorphous particles decreases to 2.6 m^2/g. For goethite α-FeOOH, the measured σBET was 92.7 m^2/g and decreases to 28.8 m^2/g. The specific surface area for hematite obtained directly by hydrolyzation at room temperature was 106.3 m^2/g.

The UV-vis-NIR absorption spectra (Kubelka–Munk function) of the synthesized samples are demonstrated in ESI Figure S2a. All hematite samples showed a sharp adsorption edge below 590 nm indicating a narrow optical bandgap. A similar trend was observed for goethite, with adsorption edge at around 520 nm. The optical bandgap values (indirect transition) for hematite were obtained from the optical absorption versus photon energy plots $(\alpha h\nu)^{1/2}$ by extrapolating linear fits of the plots to zero, as demonstrated in ESI Figure S2b [31]. The observed bandgap values for hematite samples, amorphous-800 (1.89 eV), Fe$_2$O$_3$-60 (1.97 eV) and FeOOH-800 (1.98 eV) corresponds well with literature data. The band gap values for hematite depends on the synthesis approach and are between 1.9 to 2.2 eV [32]. The bandgap value 2.33 eV for goethite (direct transition) was observed from optical absorption versus photon energy plots $(\alpha h\nu)^2$, as demonstrated in ESI Figure S2c. The observed bandgap value for goethite is in good agreement with previously reported values [25].

2.2. Photocatalytic and Photo-Fenton Activity

The visible-light photocatalytic performance of synthesized materials is demonstrated in Figure 3a by methylene blue (MB) degradation, which was evaluated from the change of the most intense absorption peak of MB at 665 nm. All catalyst materials under the study were photocatalytically inactive because the MB in light and in the absence of any catalyst material shows faster degradation due to photolysis. The C/C$_0$ value in 120 min for MB decreased by approximately 30%, while the addition of catalyst reduced the degradation to about 20%. This is attributed to the light scattering by dispersed particles which hinder the penetration of photons into the MB solution [33].

The situation was noticeably changed by H$_2$O$_2$ addition in the photo-Fenton process (Figure 3b). All materials degraded MB completely in less than 120 min. However, hematite obtained from goethite (sample FeOOH-800) destroyed over 95% of MB in only 15 min. The corresponding UV-vis spectral curves of MB solution in the photo-Fenton degradation process in the presence of hematite (FeOOH-800) sample was demonstrated in ESI Figure S3. The hematite obtained from goethite showed higher performance than polyhedrons with exposed {101} facets, which degraded MB at the same concentration in 60 min [4]. MB alone in presence of H$_2$O$_2$ under visible light degraded only by 70% in 120 min. The rate constants for MB degradation in 15 min for different materials decreased as follows: FeOOH-800 (0.2 min^{-1}) > Fe$_2$O$_3$ RT 0.07 min^{-1}) > amorphous (0.05 min^{-1}) > amorphous-800 (0.05 min^{-1}) > goethite (0.04 min^{-1}). The higher photo-Fenton activity for hematite obtained by annealing goethite (FeOOH-800) can be attributed to its high surface area, although it should not be the single reason, because Fe$_2$O$_3$ sample obtained by hydrolysation at 60 °C shows 4 times higher σBET. The other reason for the high FeOOH-800 activity could be its oblong nanoplatelet structure. It has been reported before that the recombination of photogenerated charge carriers is suppressed in one-dimensional materials [34]. Another reason for enhanced photo-Fenton activity could be the presence of nanopores in the FeOOH-800 sample, as suggested by TEM studies. The theoretical studies show that the catalytic activity can be enhanced in materials with pore sizes at the nanoscale [18].

The observed photo-Fenton activity of hematite (FeOOH-800) is a solely heterogeneous process and cannot be related to dissolution and leaching of iron from catalytic material. To prove this, we irradiated the FeOOH-800 sample in water in the presence of H$_2$O$_2$ for 24 h. After irradiation, the catalytic material was removed and MB (10 mg/L) and H$_2$O$_2$ (161 µmol/mL) were added to the water to test the homogeneous Fenton process in the dark at pH = 3. The degradation rate of MB was the same as in freshwater in the presence of H$_2$O$_2$ (ESI Figure S4). It has been also reported that the solubility of hematite at neutral conditions was extremely low (k ~ 3×10^{-42} in low ionic solution at 25 °C) [35].

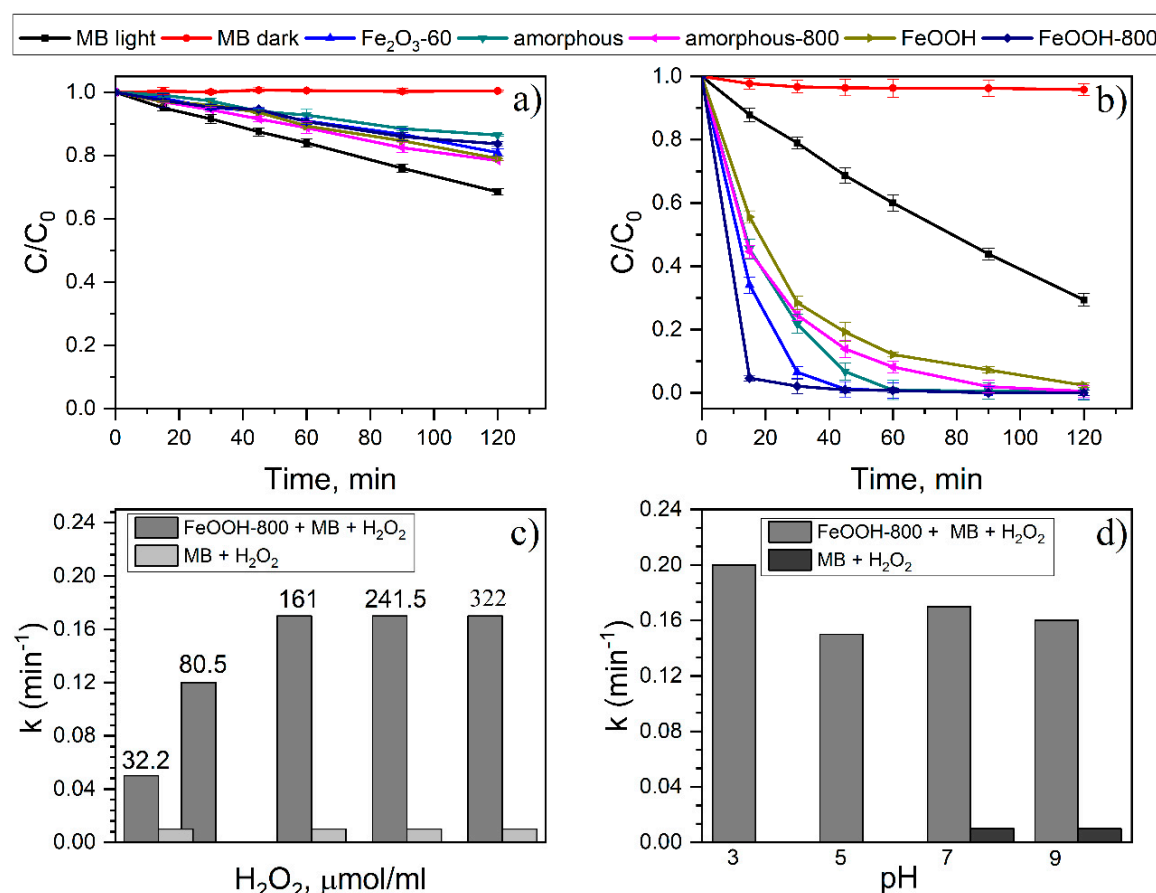**Figure 3.** The photocatalytic (**a**) and photo-Fenton (**b**) catalytic degradation of MB in the presence of different synthesized materials under visible light at neutral pH. The influence of H_2O_2 concentration (**c**) and pH (**d**) on MB degradation rate constant k in photo-Fenton process by hematite obtained by thermal transformation of goethite α-FeOOH (sample name FeOOH-800).

The photo-Fenton activity for the FeOOH-800 sample was investigated in dependence from H_2O_2 concentration (Figure 3c and ESI Figure S5). The activity increases by increasing the H_2O_2 concentration from 32.2 μmol/mL and saturates after reaching the concentration of 161 μmol/mL. The excess H_2O_2 is not good for the photo-Fenton process, because of generated $OH^{\bullet}$ radicals reacting with the excess peroxide and form H_2O and O_2 in following Equation (10) [16]:

$$2OH^{\bullet} + H_2O_2 \rightarrow 2H_2O + O_2 \tag{10}$$

The hematite photo-Fenton (FeOOH-800) catalyst shown invariable activity dependence from pH (Figure 3d and ESI Figure S6), which is expected behavior for hematite [5,18]. The rate constant for MB degradation, at pH = 3, was only 10% higher than at pH = 7. This is a clear advantage over other catalytic materials or homogeneous Fenton proceses (which require acidic conditions) and an important point for practical water treatment applications where using additional acidification may be costly and harm the catalytic material.

MB is easy to degrade; thus, we tested the photo-Fenton activity also for other more persistent dyes such as methylene orange (MO) and rhodamine-B (RhB). As can be seen in Figure 4, the degradation rate is slower, but still considerably fast if we consider that a relatively low intensity LED light source has been used in the experiments. Over 95% of MO is destroyed in 60 min, while 70% of RhB is destroyed in 120 min. The experiments show that the synthesized photo-Fenton catalysts could be used for a large variety of organic dye degradation in water treatment applications. The dyes were

degraded by OH• radicals generated in the photo-Fenton process, which is the dominant ROS in the photo-Fenton process [2].
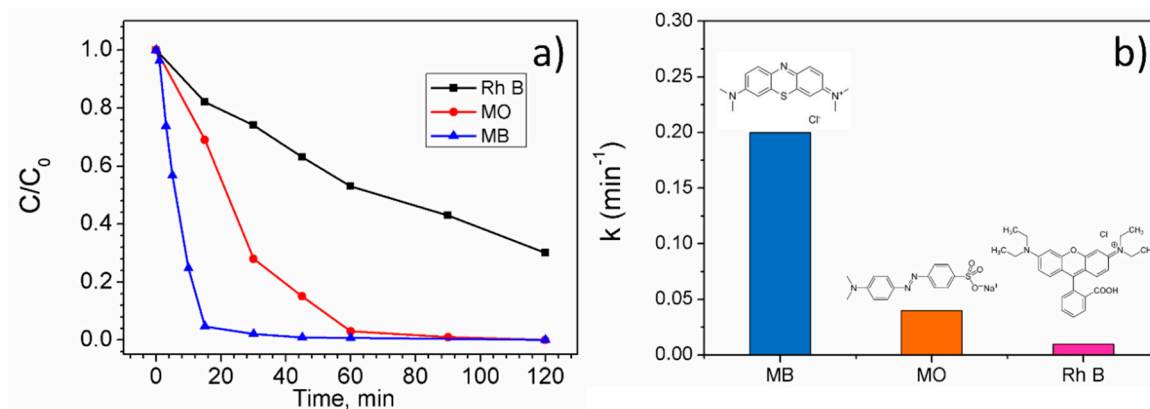

Figure 4. The relative concentration of dyes at different reaction times (**a**) and corresponding rate constants (**b**).

The synthesized hematite photo-Fenton (FeOOH-800) catalyst was completely stable under the photo-Fenton process at neutral conditions. The recycling test was carried out by degrading the MB and no decrease in the activity of hematite photo-Fenton catalyst was observed after seven cycles, as demonstrated in Figure 5, showing that the material can be safely used over and over again.
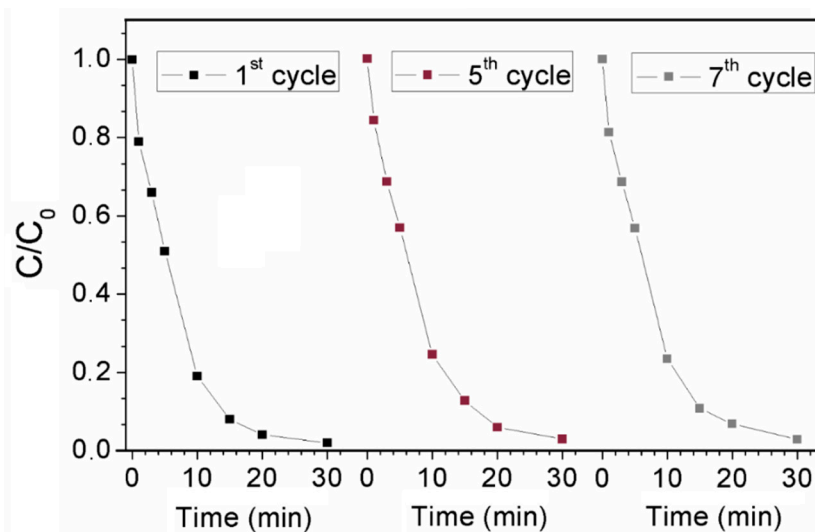
Figure 5. The recycling test for hematite photo-Fenton catalyst obtained by thermal transformation of goethite (sample name FeOOH-800) in the degradation of MB 10 mg/mL under visible light at neutral pH.

Furthermore, to test the feasibility of the hematite catalyst (FeOOH-800), the photo-Fenton test was driven in the natural sunlight. As can been seen from Figure 6, the MB was completely degraded in 10 min (rate constant k = 0.247 min^{-1}). The corresponding UV-vis spectral curves of MB solution in natural sunlight is demonstrated in ESI Figure S7. The catalytic activity of the material in sunlight was better than under LED light with an effective power density of 45 ± 3 mW/cm^2. This is attributed to the higher intensity of sunlight (70.8 mW/cm^2) during the measurement. The experiment clearly indicates that the synthesized material can be effectively used for water treatment driven by natural sunlight.
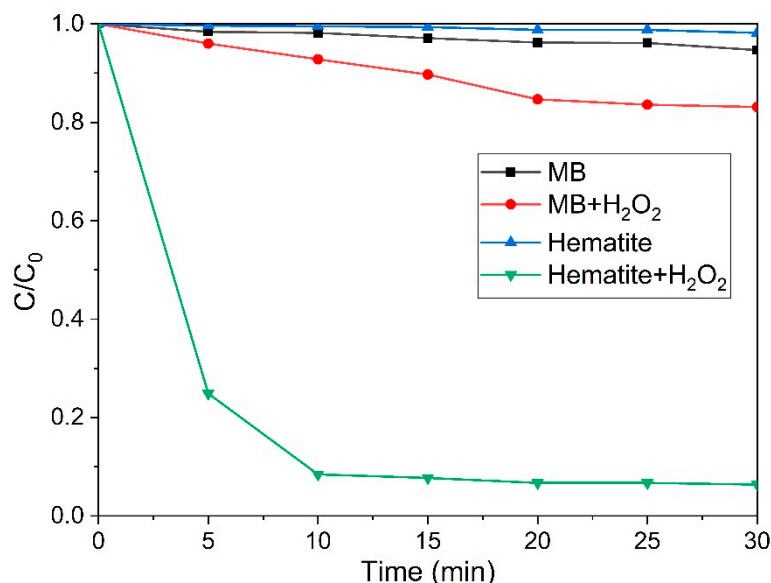
Figure 6. The degradation of MB in the presence hematite photo-Fenton catalyst (sample name FeOOH-800) under natural sunlight at neutral pH.

3. Materials and Methods

3.1. Sample Synthesis

The amorphous FeO(OH) particles were synthesized by hydrolysis of iron (iii) nitrate in 0.1 M solution using 0.5 M hexamethylenetetramine (HMTA) solution. The iron (iii) nitrate and HMTA solutions were mixed at room temperature and dark brown precipitates were collected after stirring for 10 min. The hematite and goethite nanoparticles were synthesized by hydrolysis of iron (iii) nitrate in 0.1 M solution by the addition of NaOH base solution in a equimolar ratio. The crystalline phases of precipitated iron species were controlled by changing the molarity of the NaOH solution. Hematite was obtained when 0.25 M NaOH was used to adjust the solution pH to 2.9, while goethite formed when using 0.5 M NaOH to adjust the solution pH to 12.8. After the solutions were mixed at room temperature, they were left for stirring for the next 30 min. Further, the mixtures were kept in a closed half-filled bottle at 60 °C for 72 h to observe crystallization of desired phases. After synthesis, all products were washed on a filter and dried. All reagents were chemical grade, supplied by Sigma-Aldrich (Saint Louis, MO, USA) and used as received.

To transform amorphous FeO(OH) and goethite particles to Fe_2O_3, the powders were heated in an ambient air atmosphere at 800 °C for 20 min.

3.2. Sample Characterisation

Crystalline phases of the synthesized sample powders were analyzed by X-ray powder diffraction (XRD), recorded at 2θ from 15° to 80° by using a Rigaku Ultima+ diffractometer (Prague, Czech Republic) with Cu-Kα radiation. The scanning electron microscopy (SEM) studies were performed by using a high-resolution scanning electron microscopy (SEM, Helios Nanolab, FEI, Hillsboro, OR, USA), but transmission electron microscopy (TEM) studies were performed on a Tecnai G2 F20, FEI operated at 200 kV. The specific surface area of the nanopowder was analyzed by recording nitrogen adsorption-desorption isotherms using a NOVA 1200e instrument (Quantachrome, Hampshire, UK). The optical properties were studied by measuring diffuse reflectance using a UV-Vis-NIR spectrophotometer (Shimadzu UV3700, Kyoto, Japan).

3.3. Photo-Fenton and Photocatalysis Tests

The photocatalytic and photo-Fenton activity of the synthesized samples was studied by the degradation of MB, MO and RhB in the water at neutral pH (if not specified). Before tests, sample powders were dispersed by a Hielscher UPS200 (Berlin, Germany) homogenizer in high concentration dye solution (50 mg/L) to saturate catalyst surface with particular dye and exclude the effects of adsorption in degradation tests. After keeping sample powder in high concentration dye solution for 1 h, catalyst material was centrifuged and re-dispersed in dye solution with a concentration of 10 mg/L. In photo-Fenton tests, the H_2O_2 161 μmol/mL (or another amount in some particular tests) was added to the solution. The sample powder suspensions were irradiated by a 100W light-emitting diode (LED) light source (emission band approximately 415–700 nm, i.e., 2.99 eV to 1.77 eV) with an effective power density of 45 ± 3 mW/cm^2. The tests were performed at room temperature, in closed 20 mL glass vials under constant stirring. The pH value of the suspensions was controlled by using HCl and NaOH with molar concentrations 0.1 M. The dye degradation was monitored by taking sample aliquots 1.5 mL from each suspension after a certain time interval. After centrifuging, the supernatant was analyzed by the UV-NIR spectrophotometer (Thermo Scientific Genesys 10S UV-Vis, Basel, Switzerland). In recycling tests, sample powders were centrifuged and the whole procedure was repeated from the start. The rate constant (k) of dye degradation was observed from a pseudo-first-order reaction kinetic equation, $-\ln(C/C_0) = kt$, where C_0 and C are the absorption peak intensity of dye before and after some time (t).

To estimate if there is no iron leakage from hematite during the tests and no contribution from the homogeneous Fenton process, the hematite powder was dispersed in water containing H_2O_2 161 μmol/mL and irradiated by the same LED light for 24 h. After that, sample powder was removed by centrifugation, the fresh H_2O_2 161 μmol/mL and MB 10 mg/L was added to the water and dye degradation was monitored in dark at pH 3.

4. Conclusions

The photo-Fenton activity of hematite catalytic materials, obtained by thermal phase transformation from iron-bearing particles, is highly determined by the nanoparticle precursor used. High visible light active hematite photo-Fenton catalyst was obtained by the thermal transformation from goethite α-FeOOH nanowires. The high visible light photo-Fenton activity for a particular hematite catalyst is due to the one-dimensional nanoplatelet structure and the presence of nanopores. An obtained photo-Fenton catalyst can be used for the degradation of various dyes in water under sunlight at a neutral pH and is very stable, with no sign of activity loss in seven cycles.

of scientific institutions of Latvia and the ability to attract external financing, investing in human resources and infrastructure" of the Operational Programme "Growth and Employment" (No. 1.1.1.2/VIAA/1/16/157).

Conflicts of Interest: The authors declare no conflict of interest. The funders had no role in the design of the study; in the collection, analyses, or interpretation of data; in the writing of the manuscript, or in the decision to publish the results.

References

1. Nidheesh, P. Heterogeneous Fenton catalysts for the abatement of organic pollutants from aqueous solution: A review. *RSC Adv.* **2015**, *5*, 40552–40577. [CrossRef]

2. Xiao, Y.; Deng, Y.; Huan, W.; Li, J.; Zhang, J.; Xing, M. Hollow-structured Fe_2O_3/Au/SiO_2 nanorods with enhanced and recyclable photo-Fenton oxidation for the remediation of organic pollutants. *Mater. Today Chem.* **2019**, *11*, 86–93. [CrossRef]

3. Tian, S.; Zhang, J.; Chen, J.; Kong, L.; Lu, J.; Ding, F.; Xiong, Y. $Fe_2(MoO_4)_3$ as an Effective Photo-Fenton-like Catalyst for the Degradation of Anionic and Cationic Dyes in a Wide pH Range. *Ind. Eng. Chem. Res.* **2013**, *52*, 13333–13341. [CrossRef]

4. Wang, X.; Wang, J.; Cui, Z.; Wang, S.; Cao, M. Facet effect of a-Fe_2O_3 crystals on photocatalytic performance in the photo-Fenton reaction. *RSC Adv.* **2014**, *4*, 34387–34394. [CrossRef]

5. Zhou, X.; Lan, J.; Liu, G.; Deng, K.; Yang, Y.; Nie, G.; Yu, J.; Zhi, L. Facet-mediated photodegradation of organic dye over hematite architectures by visible light. *Angew. Chem. Int. Ed.* **2012**, *51*, 178–182. [CrossRef] [PubMed]

6. Changotra, R.; Varshney, L.; Guin, J.P.; Dhir, A. Performance of hematite particles as an Iron source for the degradation of ornidazole in photo-fenton process. *J. Sol-Gel Sci. Technol.* **2018**, *85*, 203–212. [CrossRef]

7. Zhang, Y.; Zhang, N.; Wang, T.; Huang, H.; Chen, Y.; Li, Z.; Zou, Z. Heterogeneous degradation of organic contaminants in the photo-Fenton reaction employing pure cubic β-Fe_2O_3. *Appl. Catal. B Environ.* **2019**, *245*, 410–419. [CrossRef]

8. Wang, F.; Yu, X.; Ge, M.; Wu, S.; Guan, J.; Tang, J.; Wu, X.; Ritchie, R.O. Facile self-assembly synthesis of γ $Fe2O3$/graphene oxide for enhanced photo-Fenton reaction. *Environ. Pollut.* **2019**, *248*, 229–237. [CrossRef]

9. Ruales-Lonfat, C.; Barona, J.; Sienkiewicz, A.; Bensimon, M.; Colmenares, J.J.V.; Benítez, N.; Pulgarin, C. Iron oxides semiconductors are efficients for solar water disinfection: A comparison with photo-Fenton processes at neutral Ph. *Appl. Catal. B Environ.* **2015**, *166–167*, 497–508. [CrossRef]

10. Xu, J.; Li, Y.; Yuan, B.; Shen, C.; Fu, M.; Cui, H.; Sun, W. Large scale preparation of Cu-doped α-FeOOH nanoflowers and their photo-Fenton-like catalytic degradation of diclofenac sodium. *Chem. Eng. J.* **2016**, *291*, 174–183. [CrossRef]

11. Xu, Z.; Yu, Y.; Fang, D.; Xu, J.; Liang, J.; Zhou, L. Microwave-ultrasound assisted synthesis of β-FeOOH and its catalytic property in a photo-Fenton-like process. *Ultrason. Sonochem.* **2015**, *27*, 287–295. [CrossRef] [PubMed]

12. Dükkancı, M. Sono-photo-Fenton oxidation of bisphenol-A over a $LaFeO_3$ perovskite catalyst. *Ultrason. Sonochem.* **2018**, *40*, 110–116.

13. Soltani, T.; Lee, B.-K. Enhanced formation of sulfate radicals by metal-doped $BiFeO_3$ under visible light for improving photo-Fenton catalytic degradation of 2-chlorophenol. *Chem. Eng. J.* **2017**, *313*, 1258–1268. [CrossRef]

14. Sharma, R.; Bansal, S.; Singhal, S. Tailoring the photo-Fenton activity of spinel ferrites (MFe_2O_4) by incorporating different cations (M = Cu, Zn, Ni and Co) in the structure. *RSC Adv.* **2015**, *5*, 6006–6018. [CrossRef]

15. Anchieta, C.G.; Severo, E.C.; Rigo, C.; Mazutti, M.A.; Kuhn, R.C.; Müller, E.I.; Flores, E.M.; Moreira, R.D.F.P.M.; Foletto, E.L. Rapid and facile preparation of zinc ferrite ($ZnFe_2O_4$) oxide by microwave-solvothermal technique and its catalytic activity in heterogeneous photo-Fenton reaction. *Mater. Chem. Phys.* **2015**, *160*, 141–147. [CrossRef]

16. Wen, Y.; Zhao, Y.; Guo, M.; Xu, Y. Synergetic effect of Fe_2O_3 and $BiVO_4$ as photocatalyst nanocomposites for improved photo-Fenton catalytic activity. *J. Mater. Sci.* **2019**, *54*, 8236–8246. [CrossRef]

17. Yao, Y.; Cai, Y.; Lu, F.; Qin, J.; Wei, F.; Xu, C.; Wang, S. Magnetic $ZnFe_2O_4$–C_3N_4 hybrid for photocatalytic degradation of aqueous organic pollutants by visible light. *Ind. Eng. Chem. Res.* **2014**, *53*, 17294–17302. [CrossRef]

18. Wu, Z.; Zhu, W.; Zhang, M.; Lin, Y.; Xu, N.; Chen, F.; Wang, D.; Chen, Z. Adsorption and synergetic Fenton-like degradation of methylene blue by a novel mesoporous α-Fe_2O_3/SiO_2 at neutral pH. *Ind. Eng. Chem. Res.* **2018**, *57*, 5539–5549. [CrossRef]

19. Zandi, O.; Hamann, T.W. Determination of photoelectrochemical water oxidation intermediates on haematite electrode surfaces using operando infrared spectroscopy. *Nat. Chem.* **2016**, *8*, 778–783. [CrossRef]

20. Zhao, Y.; Jiangyong, H.; Chen, H. Elimination of estrogen and its estrogenicity by heterogeneous photo-Fenton catalyst β-FeOOH/resin. *J. Photoch. Photobio. A Chem.* **2012**, *212*, 94–100. [CrossRef]

21. Liu, X.; Liu, J.; Chang, Z.; Sun, X.; Li, Y. Crystal plane effect of Fe_2O_3 with various morphologies on CO catalytic oxidation. *Catal. Commun.* **2011**, *12*, 530–534. [CrossRef]

22. Mao, Y.; Wong, S.S. Size-and shape-dependent transformation of nanosized titanate into analogous anatase titania nanostructures. *J. Am. Chem. Soc.* **2006**, *128*, 8217–8226. [CrossRef] [PubMed]

23. Zboril, R.; Mashlan, M.; Petridis, D. Iron(III) oxides from thermal processes synthesis, structural and magnetic properties, Mössbaueer Spectroscopy Characterization, and Applications. *Chem. Mater.* **2002**, *14*, 969–982. [CrossRef]

24. Zhou, H.; Yi, R.; Li, J.; Su, Y.; Liu, X. Microwave-assisted synthesis and characterization of hexagonal Fe_3O_4 nanoplates. *Solid State Sci.* **2010**, *12*, 99–104. [CrossRef]

25. Šutka, A.; Järvekülg, M.; Gross, K.A.; Kook, M.; Käämbre, T.; Visnapuu, M.; Trefalt, G.; Šutka, A. Visible light to switch-on desorption from goethite. *Nanoscale* **2019**, *11*, 3794–3798. [CrossRef]

26. Wang, B.; Bin Wu, H.; Yu, L.; Xu, R.; Lim, T.-T.; Lou, X.W. Template-free formation of uniform urchin-like α-FeOOH hollow spheres with superior capability for water treatment. *Adv. Mater.* **2012**, *24*, 1111–1116. [CrossRef] [PubMed]

27. Jia, C.J.; Sun, L.D.; Yan, Z.G.; You, L.P.; Luo, F.; Han, X.D.; Yan, C.H.; Han, X.-D.; Pang, Y.-C.; Zhang, Z. Single-crystalline iron oxide nanotubes. *Angew. Chem. Int. Ed.* **2005**, *44*, 4328–4333. [CrossRef]

28. Šutka, A.; Vanags, M.; Joost, U.; Smits, K.; Ruža, J.; Locs, J.; Kleperis, J.; Juhna, T. Aqueous synthesis of Z-scheme photocatalyst powders and thin-film photoanodes from earth abundant elements. *J. Environ. Chem. Eng.* **2018**, *6*, 2606–2615. [CrossRef]

29. Cornell, R.M.; Giovanoli, R.; Schneider, W. Review of the hydrolysis of iron(III) and the crystallization of Amorphous Iron(III) Hydroxide Hydrate. *J. Chem. Tech. Biotechnol.* **1989**, *46*, 115–134. [CrossRef]

30. Johnston, J.H.; Lewis, D.G. A detailed study of the transformation of ferrihydrite to haernatite in an aqueous medium at 92 °C. *Geochim. Cosmochim. Acta* **1983**, *47*, 1823–1831. [CrossRef]

31. Murphy, A.B. Band-gap determination from diffuse reflectance measurements of semiconductor films, and application to photoelectrochemical water-splitting. *Sol. Energy Mat. Sol. Cells* **2007**, *91*, 1326–1337. [CrossRef]

32. Sivula, K.; Le Formal, F.; Grätzel, M. Solar water splitting: Progress using hematite (α-Fe_2O_3) photoelectrodes. *Chem. Sus. Chem.* **2011**, *4*, 432–449. [CrossRef] [PubMed]

33. Loeb, S.K.; Alvarez, P.J.J.; Brame, J.A.; Cates, E.L.; Choi, W.; Crittenden, J.; Dionysiou, D.D.; Li, Q.; Puma, G.L.; Quan, X.; et al. The technology horizon for photocatalytic water treatment: Sunrise or sunset? *Environ. Sci. Technol.* **2019**, *53*, 2937–2947. [CrossRef]

34. Leelavathi, A.; Madras, G.; Ravishankar, N. Origin of enhanced photocatalytic activity and photoconduction in high aspect ratio ZnO nanorods. *Phys. Chem. Chem. Phys.* **2013**, *15*, 10795–10802. [CrossRef] [PubMed]

35. Cornell, R.M.; Schwertmann, U. *The Iron Oxides: Structure, Properties, Reactions, Occurrences and Uses*; Wiley-VCH Verlag: Weinhein, Germany, 2003.